AIChE

Design of a Silicon-Based Microscale Trickle-Bed System for Singlet-Oxygen Production

Benjamin A. Wilhite and Klavs F. Jensen
Dept. of Chemical Engineering, Massachusetts Institute of Technology, Cambridge, MA 02139

Tyrone F. Hill
Dept. of Electrical Engineering and Computer Science, Massachusetts Institute of Technology, Cambridge, MA 02139

Luis Fernando Velásquez-García
Microsystems Technologies Laboratories, Massachusetts Institute of Technology, Cambridge, MA 02139

Alan H. Epstein
Dept. of Aeronautics and Astronautics, Massachusetts Institute of Technology, Cambridge, MA 02139

Carol Livermore
Dept. of Mechanical Engineering, Massachusetts Institute of Technology, Cambridge, MA 02139

DOI 10.1002/aic.11564
Published online July 21, 2008 in Wiley InterScience (www.interscience.wiley.com).

Design methodology and flow characterization of a miniaturized trickle-bed system for singlet-oxygen production via exothermic reaction of chlorine gas and basic hydrogen peroxide aqueous solution are reported. Miniaturized singlet oxygen production is accomplished by integration of several components developed for microsystems (uniform phase distributors, integrated on-chip cooling, and capillary-based phase separation) within a single device. Macroscale design equations for pressure-drop and heat-transfer rates are verified experimentally in the miniature trickle-bed reactor. Flow regime data from the present study are summarized with previous reports in microdevices and compared to conventional multiphase flow maps; these maps are found to be incapable of accurately predicting the flow regime trends within the miniaturized trickle-bed system. Operation of the silicon-based miniaturized trickle-bed reactor achieved estimated singlet-oxygen yields of 78%, comparing well with the reactor model predictions. © 2008 American Institute of Chemical Engineers *AIChE J,* 54: 2441–2455, 2008

Keywords: microreactor, gas–liquid reactor, trickle-bed, singlet-oxygen

Introduction

Microchemical systems have emerged as promising alternatives to conventional, macroscale systems for applications ranging from chemical analysis[1,2] and biological assays[3] to portable power systems[4] and small scale[5–8] and industrial-scale manufacture.[9,10] Process miniaturization and the result-

---

Correspondence concerning this article should be addressed to B. A. Wilhite at this current address: Dept. of Chemical, Materials and Biomolecular Engineering, University of Connecticut, Storrs, CT 06269. E-mail: bwilhite@engr.uconn.edu.

© 2008 American Institute of Chemical Engineers

ing reduction of characteristic length scales (e.g., hydraulic diameter, wall thickness, and catalyst size), yields order-of-magnitude increases in momentum, heat and mass transport rates, alongside equivalent gains in system safety, redundancy, and efficiency.

Fabrication of microchemical reactors via techniques developed for the integrated circuit (IC) and microelectromechanical systems industries allows the use of silicon-based materials for high-temperature applications and handling of aggressive chemistries.[11] Single crystal silicon is a strong, low-density material with a thermal conductivity comparable to that of brass, allowing production of low-weight, rapidly cooled or heated chemical reactors capable of operating under isothermal conditions. The chemical resistance of silicon can be easily augmented via thermally-grown coatings of silicon dioxide,[12] chemical-vapor deposition of silicon nitride,[13] or physical deposition of silicon carbide or nickel.[14,15]

The precision and complexity enabled by 2D photolithography methods has been employed for integration of (i) several parallel microfluidic networks,[16] (ii) in situ flow sensing with chemical reaction,[17] and (iii) multiple separate, yet coupled reacting fluids for heat-integration.[18] Additionally, microdevices combining chemical reaction with subsequent phase separations have been recently demonstrated for gas–liquid and liquid–liquid systems.[19] Recently, we completed the design and demonstration of a silicon-based micromachined device integrating (i) gas–liquid packed-bed microreactors with (ii) subsequent gas–liquid product separation, and (iii) on-chip cooling, for producing singlet-delta oxygen [$O_2(^1\Delta)$] via exothermic reaction of concentrated alkaline hydrogen peroxide solution and chlorine gas. The corrosive and unstable nature of the reagents, reaction exothermicity, and required interfacial areas made this transport-limited multiphase reaction an ideal candidate for complete process miniaturization. The resulting microdevice represents a fully miniaturized, self-contained, industrial trickle-bed reactor, requiring only external fluidic connections for operation.

This manuscript reports the design methodology employed to realize the first fully-integrated miniaturized trickle-bed reactor system, including discussion of design equations selected to specify the dimensions of each device component (inlet bifurcation and distributor, packed-bed channels, gas-liquid separator, and cooling system) and subsequent characterization of the fabricated device components to verify the design methodology. In doing so, we expand upon previous reports on the microscale singlet-oxygen generator, which focused upon modeling analysis of the packed-bed reaction microchannels,[20] device fabrication and packaging,[13] and IR-spectroscopic analysis of singlet-oxygen production over a range of operating conditions.[21] The case study for integrated gas–liquid microreactor design presented here demonstrates a useful design methodology for creating integrated microreactor systems for multiphase chemical applications.

Applications for singlet-delta oxygen

Singlet-delta oxygen is a spin-excited molecule in which the number of valence electrons in each spin state is balanced, resulting in an energy difference of 94.1 kJ mol^{-1} between the excited singlet-delta and ground states.[22] This additional energy content of singlet-delta oxygen makes it a valuable reagent for multiple chemical processes, including endoperoxide formation for organic synthesis[23] and photodynamic cancer therapies.[24] The most demanding use of singlet-delta oxygen is as a pumping medium for iodine-based flowing gas lasers, where high-energy laser outputs necessitate efficient generation of singlet-delta oxygen at maximum yields.

The chemical oxygen iodine laser (COIL) has emerged as a promising alternative to carbon dioxide lasers[25,26] for applications ranging from automobile manufacture[27] to automated decontamination and decommissioning (D&D) of nuclear reactors,[28] owing to its improved power outputs, wavelength characteristics, compatibility with glass optics and scalability from outputs of 1 kW to in excess of 1 MW.[29,30] The COIL system is comprised of a chemical reactor for generating singlet-delta oxygen, followed by a supersonic nozzle for rapid introduction and cooling of the iodine lasing medium, followed by the optical cavity and downstream pressure recovery (pumping) system. Complete details of a proposed fully miniaturized COIL system (the MIT μCOIL) are given elsewhere.[20] The primary challenge in the design and operation of the overall COIL system is the safe and reliable production of the singlet-delta oxygen in sufficient quantity and quality in a compact, lightweight reactor.

Challenges to singlet-delta oxygen production

Although a variety of reaction schemes for chemical generation of singlet-delta oxygen exist,[31–33] the two-phase reaction of basic hydrogen peroxide (BHP) and chlorine gas is still the preferred technology for COIL systems, owing to its capability for generating large amounts of singlet-delta oxygen with short reaction times. BHP is prepared from equal parts 50 wt % H_2O_2 and 50 wt % KOH; the resulting solution is an effervescent, viscous fluid that decomposes rapidly at temperatures above 30°C. The overall reaction of BHP with chlorine to produce singlet-delta oxygen and heat is

$$\begin{aligned} H_2O_{2(l)} + 2KOH_{(l)} + Cl_{2(g)} \rightarrow 2H_2O_{(l)} + 2KCl_{(l)} \\ + O_2(^1\Delta)_{(g)} + 110\ \text{kJ/mol}. \end{aligned}$$

The kinetics of the liquid-phase reactions are rapid, resulting in an overall reaction limited by mass transfer of chlorine across the gas-liquid interface, necessitating large interfacial areas within the reactor. Existing singlet-oxygen generator designs have achieved large gas-liquid contacting areas using wetted wall,[34] gas-sparger,[35] and liquid-spray reactors.[36]

In addition to realizing large interfacial areas for chlorine mass transport, SOG designs must be capable of high rates of heat removal for safe and efficient operation. A primary safety challenge to COIL systems is preventing BHP from overheating, which leads to rapid decomposition at temperatures above 30°C. During operation, the reaction temperatures are maintained at 258 K–268 K for safety and to minimize water vapor content in the gas product stream; water vapor leads to deactivation of the excited-state species.[37] These challenges are exacerbated by the high heat of reaction for the singlet-delta oxygen generation. Increased surface area-to-volume ratios achievable in microchemical systems

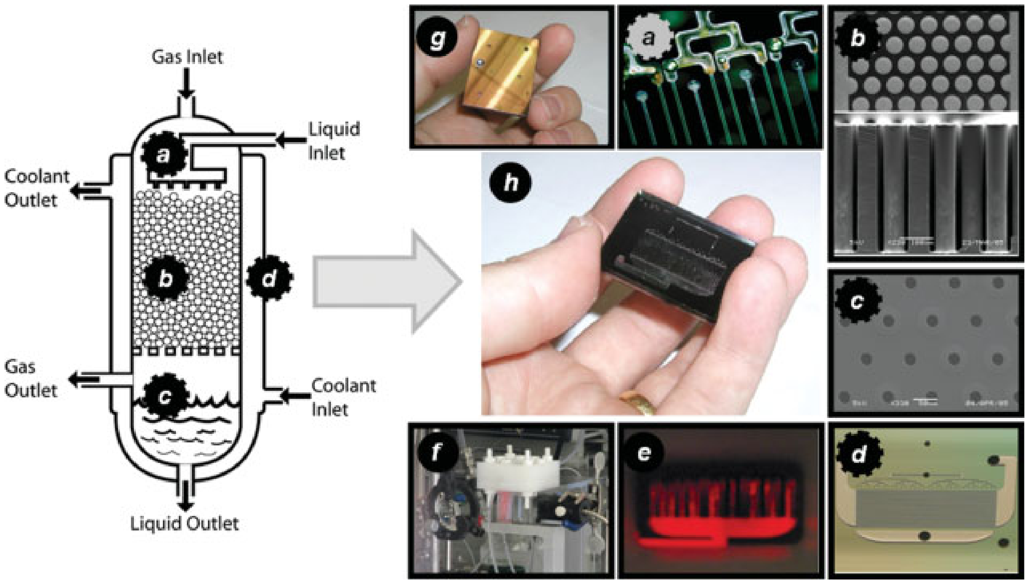

Figure 1. The miniaturized trickle-bed reactor system.

(a) Gas–liquid distributors with bifurcations and pressure-drop channels; (b) the micromachined structured packed-bed, top and side-views; (c) gas–liquid separator pores for disengagement via capillary mechanism; (d) cooling channels for heat extraction; (e) singlet-oxygen production, visually confirmed via dimol emission at 634 nm; (f) the packaged microdevice with optical cuvette for measurement of singlet-oxygen concentration via monomol emission at 1280 nm; (g) the completed microdevice, top view showing distributor, packed-beds and gas–liquid separator; (h) the completed microdevice, backside view showing inlet and outlet ports for fluidic connections. Images in (b), (c), (d), (e), (f) from Velasquez-Garcia et al., 2007.[13] [Color figure can be viewed in the online issue, which is available at www.interscience.wiley.com.]

offer the superior heat and mass transport required by this reaction, as compared to macroscale counterparts.[38]

In light of the highly toxic, corrosive, and unstable reagents involved in this reaction network, the additional safety and redundancy of microchemical systems are a welcome alternative to conventional systems with reaction volumes equivalent to 1–10 kW output. Perhaps most importantly, miniaturization of the entire COIL system is expected to result in significant reduction in overall system weight and volume necessary for next-generation transportable systems.[20]

Silicon-based microchemical systems appear perfectly suited for high-capacity singlet-delta oxygen production, for use either by COIL systems or by organic synthesis processes.[11] Silicon construction and micrometer-scale heat transport lengths allow isothermal operation even at high reaction rates; gas and liquid distributors allow scale-out of individual reaction channels while minimizing variations in distribution uniformity (common to conventional system scale-up) for greater design flexibility[39]; and capillary-based gas-liquid separators[40] allow disengagement of the gas product from the liquid phase immediately after reaction to minimize the deactivation losses. A modeling study of the microscale singlet-oxygen generator predicted superior performance of the microreactor and the μCOIL system, as compared to the state-of-the-art macroscale systems.[20] The present manuscript details the design of a prototype singlet-oxygen generator (including structured reaction channels, distributors, gas–liquid separator, cooling channels, and packaging), with an emphasis upon verifying design models/expressions employed for each microsystem component. Overall system performance is also presented, with emphasis upon comparing observed, multiphase hydrodynamics within structured microscale packed-beds with conventional predictive maps. Complete details of microfabrication methods and IR-spectroscopic analysis of overall singlet-delta oxygen production by the resulting microdevice are provided by the authors elsewhere.[13,21]

Design of Microscale Jacketed Trickle-Bed System

Conventional gas–liquid reactor systems are comprised of (i) a fluidic distributor for achieving uniform mixed inlet flow, (ii) a randomly or structured packed bed to provide maximum interfacial contact area, (iii) cooling or heating jacket for temperature control, and (iv) a disengagement volume for splitting reactor effluent into separate product phase(s). Although each of these individual tasks has been demonstrated earlier in silicon-based microsystems,[38–41] this manuscript presents the first bottom-up design of an integrated microscale trickle-bed system, combining all of these tasks into a single, compact, and efficient microdevice, illustrated conceptually in Figure 1 and by design in Figure 2.

The design methodology illustrated in Figure 2 centers around an isothermal model of the chemical reactor. In this manner, all subsequent component designs are based upon an optimal reactor design, independent of arbitrary device size constraints. Optimal bed properties obtained from the reactor model dictate post (structured packing) diameters and spacing, whereas individual reaction channel capacities dictate the number of identical channels necessary to meet the overall target flow capacities. Spacing between reaction channels is selected based upon ease of microfabrication; nominally a

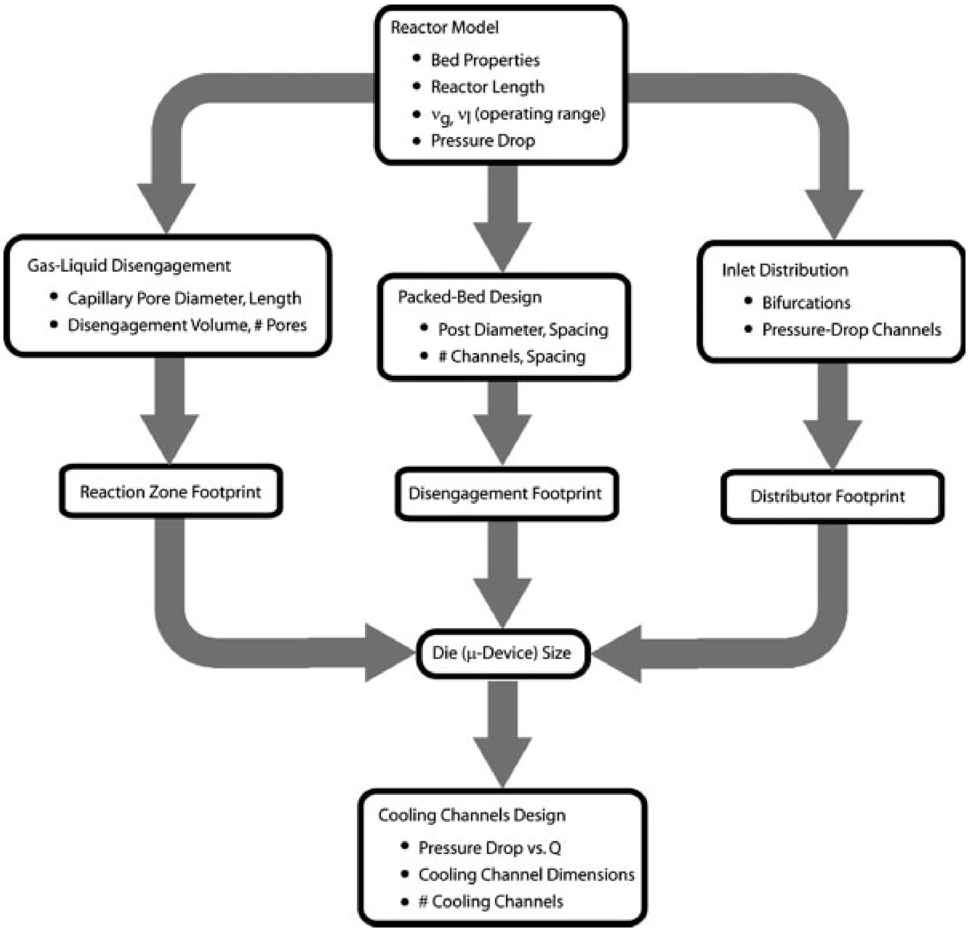

Figure 2. Design flowsheet for microscale trickle-bed system.

spacing of 100 μm represents a reasonable balance between device compactness and fabrication reproducibility. The number of parallel reaction channels along with the individual channel capacities dictates inlet bifurcation design, whereas the reaction channel pressure drop dictates the design of pressure-drop constrictions. Downstream of the reaction region, net gas and liquid effluent and target outlet (plenum) pressure guides the design of the gas–liquid disengagement region. Once dimensions and necessary design parameters for the packed-bed reaction channels, distribution region, and disengagement region are determined, individual region blueprints or lithography masks can be developed, which in turn dictate the footprints of each region. When combined, these three regions define the overall die size for an integrated microdevice where all the three regions are placed on the frontside of the microdevice. Lastly, cooling channels are designed for placement on the backside of the microdevice, to ensure isothermal operation and adequate heat removal.

Trickle-bed reactor model

A one-dimensional plug-flow reactor model (neglecting axial dispersion) was formulated to describe gas–liquid reaction and gas-phase deactivation in a single, microscale packed-bed. Axial dispersion was neglected for initial design

Table 1. Design Parameters Obtained from MIT μCOIL Optimization Study

Parameter	Range	Predicted Optimum	Experimental
Bed cross-sectional area	1.95×10^{-7} m^2		
Packing diameter	70×10^{-6} m		
Bed porosity, dimensionless	0.40		
He:Cl$_2$ gas inlet rate, 32-channel device	4.2–430 cm^3 min^{-1} (at STP)	175 cm^3 min^{-1} (at STP)	25–175 cm^3 min^{-1} (at STP)
BHP liquid inlet rate, 32-channel device	0.75–7.50 cm^3 min^{-1}	3 cm^3 min^{-1}	0.5–2.5 cm^3 min^{-1}
Packed bed length	0–1 cm	0.516 cm	0.61 cm
Packed-bed outlet pressure	3–40 kPa	6.2 kPa	5–35 kPa
$N_{Bo_{Cl_2}}$ at 40 kPa	1.8–180	70	10–70
$N_{Bo_{O_2}}$ at 40 kPa	1.2–120	50	8–50
$N_{Bo_{O_2H^-}}$ at 40 kPa	10^4–10^5	5×10^5	8×10^4–4×10^5

studies to facilitate design optimization at a minimum of computational cost. Owing to rapid liquid-phase kinetics, the overall rate of the reaction can be assumed to be equal to the rate of gas–liquid mass transport, and the mass transfer coefficient estimated from the limiting liquid-phase kinetics. The model assumed a liquid-fraction $\varepsilon_l = 0.08$ (with total void fraction of $\varepsilon = 0.40$). Gas–liquid interfacial area was estimated at $a = 5000\ \mathrm{m}^{-1}$ based upon previously reported values in similar structured microscale packed beds by Losey et al.[38] This model was originally developed as part of a larger design study of a microscale Chemical Oxygen Iodine Laser (μCOIL) system, and complete details of the model formulation are provided elsewhere.[20] Results of this modeling analysis are summarized in Table 1. Although an optimal bed length of 0.516 cm was obtained from model analysis,[20] an experimental bed length of 0.61 cm was selected to provide additional residence time to ensure sufficient conversion over the entire range of gas and liquid throughputs.

Reactor bed design

The bed geometry was selected to match the modeling results summarized in Table 1. In order to achieve overall device capacities in excess of 1 mL min^{-1} (for effective fluid handling and product analysis), each integrated device is designed to contain 32 parallel packed-bed channels. Individual packed bed dimensions were 650 μm in width by 300 μm in depth, with structured posts serving as the packing media. Structured two-dimensional packing elements were chosen over randomly dumped beds for greater ease of manufacture and operation. Each bed was packed with $\sim 5 \times 10^3$ identical, 70 μm diameter posts placed in a regular hexagonal pattern with identical pore throats of 20 μm, corresponding to an overall bed porosity of 0.40 (Figure 1b). Post diameters correspond to a bed width-to-packing diameter ratio of ~8:1, generally considered the minimum for uniform flow distribution in conventional packed-bed systems.[42] Larger bed-to-packing diameter ratios were not implemented to maximize device yield and decrease fabrication complexity.

Design of gas and liquid distribution

A critical challenge to the scale-up of microchemical systems is appropriate design of fluidic distributors[38,39,43] to ensure consistent reagent supply to each microchannel. Although simple bifurcated gas and liquid inlets split individual external feeds amongst multiple reaction channels (Figure 1a), minor fluctuations in pressure drop associated with each flow path may still result in significant distribution nonuniformity.[38] To ensure uniform gas and liquid distribution to each reaction channel, individual reaction channels are connected to the inlet bifurcation arrays via two shallow pressure drop channels for gas reagent and a single shallow pressure drop channel for liquid reagent, following Wada and coworkers[39] (Figure 1a).

Pressure-drop channels were designed to achieve a 3-fold greater pressure drop than downstream reaction channel pressure drops, to ensure that fluid flowrates are dominated by the pressure drop associated with the pressure-drop channel; that is, distribution is unaffected by downstream pressure fluctuations. Further pressurization of the BHP supply was not considered feasible in light of safety considerations. Pressure-drop was determined from the Hagen-Pouiseille equation for an incompressible fluid,

$$\Delta P_{\mathrm{pdc}} = \frac{128\mu_l \cdot L_{\mathrm{pdc}} Q_{\mathrm{pdc}}}{\pi \cdot d_{\mathrm{pdc}}^4} \tag{1a}$$

where μ_l is the fluid viscosity, L_{pdc} is the length the pressure-drop channel, Q_{pdc} is the capacity of a single pressure-drop channel, and d_{pdc} is the hydraulic diameter of a single pressure-drop channel. Pressure-drop channel widths of 25 μm and depths of 20 μm were selected as minimum feature sizes without affecting overall device yield or introducing plugging challenges during operation. Optimum operating conditions predicted from the design optimization study corresponded to a pressure drop of 360 torr across the reaction channel (Table 1). For a target pressure drop of 1200 torr across the pressure-drop channel at optimal operating conditions, a length of 2.5 mm is obtained from Eq. 1a.

Design of capillary gas–liquid separator

Macroscale gas–liquid reactors employ downstream phase separation by exploiting differences in density, primarily via gravity separation. In microscale systems, capillary forces compete with or dominate gravity forces, limiting the use of conventional density-separation methods for gas–liquid disengagement. For this reason, a gas–liquid separator based upon capillary action, originally developed by Günther et al.,[40] was used to separate the effluent stream exiting the array of 32 packed-beds.

The separator consists of a collection conduit, the floor of which is patterned with an array of parallel capillary pores for selective removal of the liquid phase from the gas–liquid effluent (Figure 1d). Individual pores must be small enough to maintain sufficient capillary pressure to resist gas invasion, while remaining large enough to provide useful liquid removal rates (Figure 3). Separation is accomplished by applying a pressure drop across the capillary channels smaller than the maximum pressure that the meniscus can withstand before breakup, so the gas phase does not get through the capillary. The upper bound of this pressure calculated from the Laplace-Young Equation:

$$\Delta P_{\mathrm{cap}} = \frac{4\sigma}{d_{\mathrm{cap}}} \cos\theta \tag{2}$$

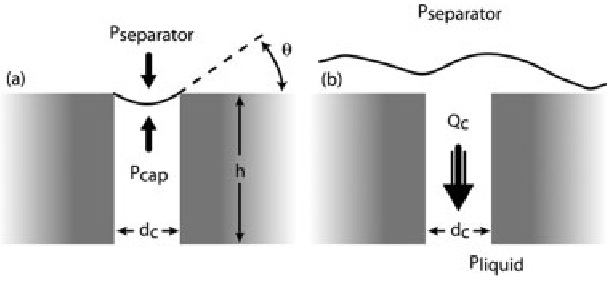

Figure 3. Illustration of capillary separator design.

(a) Liquid-filled stagnant (inactive) separator pores resist gas invasion when $P_{\mathrm{separator}} < P_{\mathrm{cap}}$; (b) liquid-filled flowing (active) separator pores withdraw liquid at rates determined from Hagen-Pouiseille equation.

where σ is the liquid surface tension, θ is the wetting angle, and d_{cap} is the diameter of a single capillary pore. The capacity of a single pore in the separator is then calculated from the Hagen-Pouiseille equation,

$$Q_{cap} = \frac{\pi \cdot d_{cap}^4 \cdot \Delta P_{sep}}{128 \mu_l \cdot L_{cap}} \tag{1b}$$

where ΔP_{sep} is the actual pressure drop applied across the capillary separator and L_{cap} is the pore length. A capillary pore length of 300 μm was selected to accommodate both the reactor bed and the separator on the same 625 μm thick silicon substrate. Capillary diameters were chosen to be 25 μm, corresponding to a maximum allowable pressure differential of 117 torr, assuming that BHP's surface tension is equivalent to that of water (73 dynes cm^{-1}) and also assuming negligible wetting angle (corresponding to water on silicon nitride). Actual surface tension and wetting angle data for BHP and silicon were unknown. In light of this potential source of error, the operating pressure drop across the separator was targeted for 25% of the predicted capillary pressure (30 torr), to ensure desired performance during operation. This corresponds to a single-pore liquid removal rate of 1.7×10^{-5} cm^3 s^{-1} (Eq. 1b). Operation at the maximum planned liquid flowrate of 0.123 cm^3 s^{-1} (determined from modeling analysis) requires $\sim$7200 capillary pores. Operation at the optimum liquid flowrate of 0.0492 cm^3 s^{-1} requires only $\sim$2800 pores. However, prewetting of the separator device allows pores to remain liquid-filled while not in use, thereby preventing gas penetration into the liquid effluent (Figure 3). Prewetting of the separator is a crucial step to run the microscale reactor system. Analysis of the working conditions used to gather the IR data showed that only a small fraction of open pores ($<$5%) are needed to suck the singlet oxygen to the liquid by-products outlet instead of the proper singlet exit port.[21]

Design of cooling channels

Once the reaction channels, gas–liquid inlets, and gas–liquid disengagement regions were designed, the overall die size of the microreactor was set to 3.6 cm × 2.8 cm to accommodate these features and feed/outlet ports on the device backside. The final design step was to specify the cooling channel geometry to maintain the desired chip temperatures of 273–283 K in the presence of heat addition from both the ambient environment and singlet-oxygen production. At maximum design flowrates of 8×10^{-5} mol Cl_2/s, the corresponding heat production via reaction is 8.8 W, whereas optimal operating conditions correspond to a heat release rate of 3.5 W. For a chip design temperature of 268 K, heat losses from the microdevice via natural convection are estimated at $\sim$0.50 W.

The Nusselt number corresponding to coolant flow through a single microchannel was estimated via the correlation of Sieder and Tate[44] for laminar flow (Reynolds number $N_{Re} < 2100$) through a cylindrical pipe, assuming constant coolant viscosity:

$$N_{Nu} = \frac{h_a D}{k} = 1.86 \left(N_{Re} \cdot N_{Pr} \cdot \frac{D}{L} \right)^{1/3} = 1.86 \left(\frac{4 \rho C_p Q}{k L_c \pi} \right)^{1/3} \tag{3}$$

Equating the maximum heat flow out of the chip with heat flow into the coolant (assuming steady-state operation) yields an expression, which is solved for the coolant outlet temperature and the heat duty of the cooling channel:

$$q^- = h_a \pi D_c L_c \left(T_{wall} - \left(\frac{T_{c,in} + T_{c,out}}{2} \right) \right) \tag{4a}$$

$$q^+ = Q_c \rho_c C_p \left(T_{c,in} - T_{c,out} \right) \tag{4b}$$

$$\frac{2T_{wall} - T_{c,in}(1-\alpha)}{(1+\alpha)} = T_{c,out}, \quad \text{where} \quad \alpha = \left(\frac{\rho_c Q_c C_p}{\pi L_c N_{Nu} k} \right) = \left(\frac{\rho_c^{2/3} Q_c^{2/3} C_p^{2/3}}{6.33 \cdot L_c^{2/3} k^{2/3}} \right) \tag{4c}$$

The corresponding pressure drop for a given coolant capacity is given by the Hagen-Pouiseille equation,

$$\Delta P_c = \frac{128 \cdot L_c \mu_c Q_c}{\pi d_c^4} \tag{1c}$$

For a single cooling channel at fixed coolant flowrate, inspection of Eqs. 3, 4, and 1c illustrate that heat removal is not a direct function of hydraulic diameter, and that $q \propto (L_c)^{2/3}$ while $\Delta P \propto L_c$. Thus, as flow length is increased, the amount of energy required for pumping outpaces the rate of heat removal. The energy required to flow the coolant goes mainly to pay for the viscous losses, which produce heating of the coolant, directly interfering with its heat removal capacity. Therefore, the design of an efficient heat exchanger should make provisions for its heat removal capacity to be substantially larger than the heating implied in flowing the coolant. The hydraulic diameter indirectly influences net heat removal by dictating the number of cooling channels that can be incorporated into the microdevice. For a fixed volume available for channel placement, geometry shows that $q \propto n_{channels} \propto (d_c)^{-2}$ whereas from Eq. 1c we see that $\Delta P \propto (d_c)^{-4}$. Thus, selection of hydraulic diameter represents an indirect balance between heat removal rates and pressure drop.

The established die size (3.6 cm × 2.8 cm) provides a 2.2 cm × 8.5 mm footprint for incorporation of cooling channels of 300 μm depth (Figure 1d). Cross-flow operation of cooling channels (alignment of channels perpendicular to reaction channels) was selected to ensure maximum uniformity of reactor temperature along a given reaction channel, and to accommodate coolant port placement compatible with reactant and effluent port placements. Channel dimensions of 300 × 300 μm (D_c = 339 μm) × 22 mm allow placement of 19 separate cooling channels on-chip, with single-pass operation of coolant channels (L_c = 22 mm) to maintain low pressure drops.

Design calculations were performed for a target coolant inlet temperature of 258 K and chip temperature of 268 K. Design calculations assumed the use of Syltherm© XLT Fluid as a coolant. The physical properties of Syltherm© XLT Fluid are summarized in Table 2. For a net coolant capacity of 137 cm^3 min^{-1}, N_{Re} = 157.9, and N_{Nu} = 8.04, the target heat removal rate of 4 W is achieved at a pressure drop of 21 kPa. For a net coolant capacity of 237 cm^3

Table 2. Properties of Coolant for Design of Heat Exchanger

Property (at -10°C)	Value
Density	870.11 kg m^{-3}
Specific heat	1.572 kJ kg^{-1} K^{-1}
Thermal conductivity	0.1171 W m^{-1} K^{-1}
Viscosity	2.49×10^{-3} Pa s^{-1}
Prandtl number	33.4

min^{-1}, a heat removal rate of 10 W can be achieved at a pressure drop of 69 kPa, corresponding to the maximum pressure drop achievable by the chiller/recirculator employed in the experimental procedure.

Experimental

Chip fabrication

The integrated microscale trickle-bed system was fabricated from two individually micromachined silicon layers of thickness 625 μm each, capped with a 2 mm Pyrex layer to enable optical access to the packed-bed and capillary separator. A cross-sectional schematic of the microdevice is presented in Figure 4a, alongside optical images of the backside of the chip, the frontside of the chip, and the internal cooling channel features (Figures 4b–d). The fabrication process relies heavily on deep reactive ion etching (DRIE), fusion bonding, and anodic bonding methods to construct the device in silicon. Subsequent deposition of a conformal layer of LPCVD-deposited silicon-rich nitride provided suitable protection from reactant and by-product corrosion. Complete details of the fabrication process are presented elsewhere.[13]

Testing apparatus

The testing apparatus is shown schematically in Figure 5. Gas delivery was provided via mass flow controllers, connected with a mixing tee and downstream pressure transducer for measuring delivery pressure. The gas outlet flow path included (i) an optical cuvette for measurement of singlet-oxygen emission via spectroscopy, (ii) a cryo-trap for chlorine and moisture removal, (iii) a sampling port for mass spectroscopy, (iv) a back-pressure valve for control of gas outlet pressure, and lastly (v) a corrosion resistant vacuum pump. The liquid supply reservoir was a glass-lined, jacketed, stainless steel pressurized reservoir (PARR), pumped to the chip/chuck assembly by constant-pressure helium gas displacement using separate mass-flow and back-pressure controllers. The liquid outlet flow was collected in a jacketed three-neck glass flask, maintained at constant vacuum pressure via a back-pressure controller connected to the vacuum pump. In both the gas and liquid outlet vacuum lines, glass cryo-traps were employed to remove any moisture or chlorine vapor upstream of the vacuum components. Both the liquid inlet and outlet reservoirs were maintained at sub-ambient temperatures using a chiller/recirculator, which also supplied coolant flow to the chip. Coolant supply rates to the liquid reservoirs and chip were controlled using flowmeters. Thermocouples provided constant monitoring of chip and reservoir temperatures during experimentation. The present design employs a single on-chip thermocouple well for monitoring silicon substrate temperature. Fluidic connections to the glassware and the packaging chuck were made using PTFE tubing. Ultra-high purity gases (>99.999%) were used in the experiments. The entire experimental apparatus, with the exception of the coolant recirculator/chiller, was contained

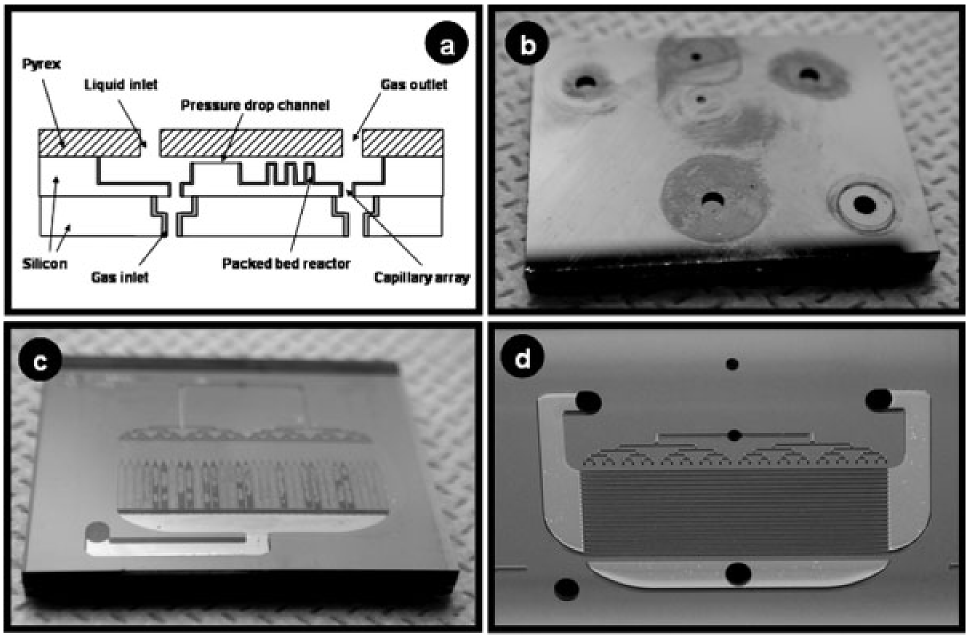

Figure 4. Microdevice fabrication.

(a) schematic view of device cross-section; (b) backside of completed microdevice identifying individual inlet and outlet ports; (c) frontside view of completed microdevice; (d) internal cooling channels.

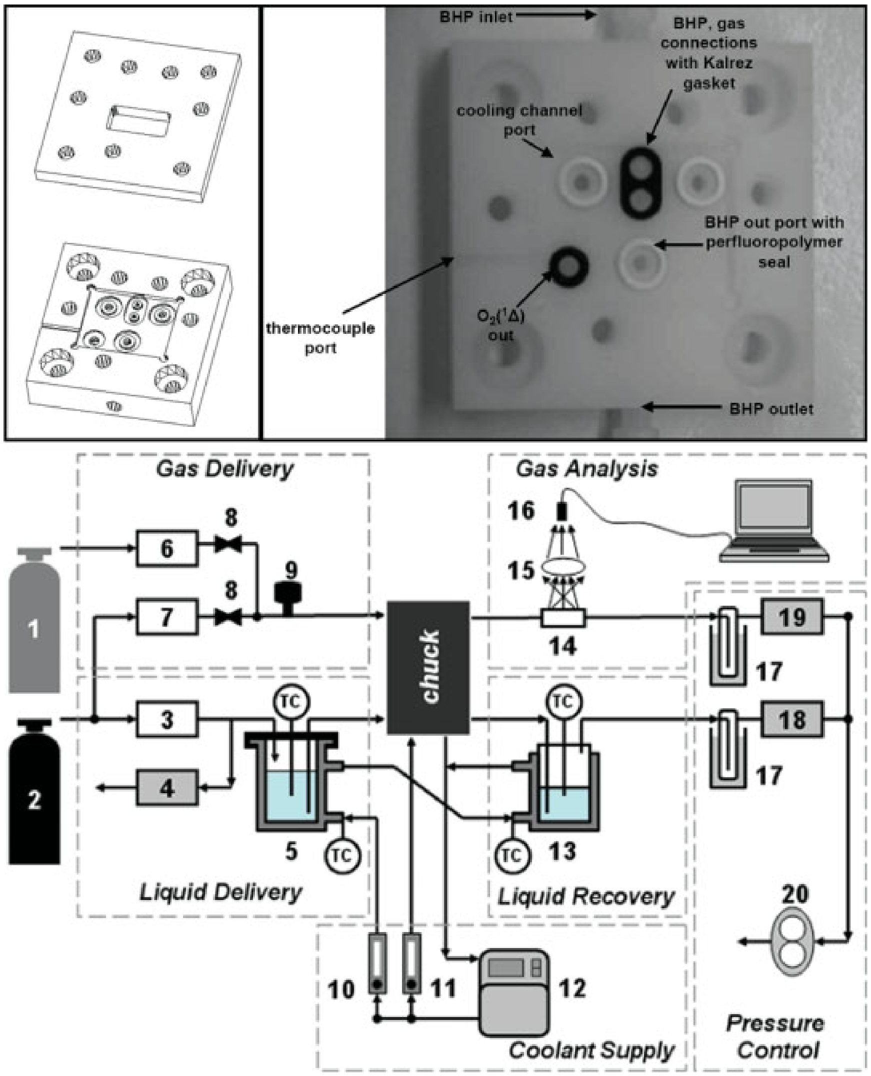

Figure 5. Testing methodology.

(a) packaging chuck, showing inlet and outlet ports, from Velasquez-Garcia et al., 2007[13]; (b) experimental apparatus: (1) Chlorine cylinder; (2) Helium cylinder; (3) Helium mass flow controller; (4) back-pressure controller; (5) liquid supply reservoir; (6) Helium mass flow controller; (7) Chlorine mass flow controller; (8) toggle valve; (9) pressure transducer; coolant flow controllers for (10) liquid delivery/recovery and (11) microdevice; (12) chiller/recirculator; (13) liquid recovery reservoir; (14) optical cuvette; (15) focusing lense; (16) spectrometer; (17) LN moisture traps; (18) liquid removal pressure controller; (19) gas outlet pressure controller; (20) vacuum pump. [Color figure can be viewed in the online issue, which is available at www.interscience.wiley.com.]

within a ventilated enclosure to minimize the hazard of chlorine exposure. Complete details of the testing apparatus are presented elsewhere.[21]

Spectroscopic measurement of singlet-delta oxygen yield and chlorine conversion

In all experiments, singlet-delta oxygen yield was measured via photon emission spectroscopy. Quantitative measurement of singlet-delta oxygen is obtained from monitoring the decay of solitary $O_2(^1\Delta)$ molecules into the triplet state, which produces photons at 1268 nm. Spectroscopic measurement of singlet-delta oxygen concentration was performed in collaboration with Physical Sciences (Andover, MA). The test cell was a rectangular quartz cuvette connected to the gas outlet by a 0.4 cm diameter quartz tube. Collimated optics sampled a cylindrical cross section of the cuvette, yielding a 1.1 cm field of view. A liquid nitrogen cooled InGaAs array spectrometer was used to analyze photons from the spontaneous emission. The intensity of the spectrometer signal was calibrated to the spectral radiance of a blackbody source at 1000 K. Complete discussion of this analysis technique is presented by Rawlins et al.[45] Complete details of the implemented spectrometric oxygen diagnostics are presented elsewhere.[21]

Packaging of completed microdevice

A consistent challenge to microchemical systems is providing fluidic and/or electronic connections to the microdevice via packaging. Packaging strategies include sealing fluidic connections to the microdevice surface with chemical-resistant epoxies[46] or metal-solder bonds,[47] or compression-sealing with a fluidic chuck containing chemically resistant o-rings or gaskets.[39] Both chlorine gas and BHP solution are incompatible with soldering materials, whereas epoxies proved unstable over long operating times. For these reasons, a packaging system consisting of a fluidic chuck and clamping plate was used (Figures 5b, c).

Both the chuck and the clamping plate were machined from Tefzel®, and Kalrez o-rings and gaskets were used to connect the chip to Teflon tubing to meet the structural and chemical performance requirements. The clamping plate of the package has an opening for optical access to the reactor bed and separator during operation. In order to minimize deactivation of product singlet-oxygen via wall collisions, glass materials were employed for the gas outlet.[37] Complete details of the device package are presented elsewhere.[13]

Experimental procedures

For each experiment, a 1/32 in. O.D. thermocouple (Omega) was installed in the on-chip port for monitoring chip temperature, the microdevice was sealed within the chuck assembly, and all fluidic connections were attached. The chuck-chip assembly were then secured in place, and the spectroscopy optics were aligned to the optical cuvette. The chiller/recirculator were then switched on, and coolant flow to both liquid reservoirs and the on-chip cooling channels were set to desired rates. Sufficient time was allowed for the chiller temperature to reach an operating temperature of 243 K. Owing to heat addition through insulated coolant lines and flowmeters, this corresponded to a coolant temperature of 258 K at the chip inlet. BHP solution was prepared as follows. First, 100 cm^3 of 50 wt % aqueous solution of KOH was prepared from distilled water and 66 g KOH pellets (Fisher) in a volumetric flask. Meanwhile, 50 cm^3 of 50 wt % hydrogen peroxide aqueous solution (Aldrich) was poured into the liquid feed reservoir and cooled to 258.15 K. KOH solution was added in 5 cm^3 quantities, allowing sufficient time for solution temperature to return to 258 K between each addition, to a total of 50 cm^3. The BHP feed reservoir was then sealed and pressurized with helium gas to the desired delivery pressure, thus initiating liquid flow to the cooled microchip. Gas flow was initiated by opening helium flow to a rate of 50 standard cm^3/min. Liquid flow was maintained by delivering helium gas to the BHP reservoir at a constant displacement pressure of 200–400 kPa. Once both liquid and gas supply to the chip were verified, the vacuum pump was turned on, and the vent valves were closed, allowing the system to pump down to operating pressures. Gas outlet pressures were typically between 10 and 20 kPa, with liquid outlet pressures nominally set to 5 kPa less than gas outlet pressure. During pump-down, care was taken to ensure that the gas outlet pressure remained greater than the liquid outlet pressure, to avoid suction of liquid reagent into the gas outlet and downstream optics. Once both gas and liquid outlets reached steady operating pressures, reaction was initiated by blending chlorine gas into the gas feed at a mole fraction of 25%. Before chlorine introduction, the ventilated enclosure was closed and sealed to protect against chlorine exposure. Progress of the reaction was visually confirmed via red glow corresponding to $O_2(^1\Delta)$ dimol emission (Figures 1e, f).[13]

Results

Pressure-drop measurements

Initial experiments employing helium and distilled water at ambient temperature and outlet pressure were performed to measure single and two-phase pressure drops across the miniaturized distributor and packed-bed to verify design equations. Single-phase pressure drops were obtained assuming a chip outlet pressure of 101.3 kPa while monitoring delivery pressures. A parity plot of predicted pressure drops calculated from the Ergun equation for single-phase flow[48] and employing the correlation of Larkins et al.,[49] for two-phase flow verifies the accuracy of macroscale packed-bed pressure drop equations for describing the miniaturized packed-bed (Figure 6a).

Characterization of cooling channels

Preliminary experiments were also performed to estimate heat losses to ambient from the chip in the absence of chemical reaction and to estimate heat transfer coefficients within the microdevice. Although experiments in the absence of chemical reaction limit the resolution of heat transfer measurements, they alleviate the greater uncertainty associated with the estimating reaction heats. Two separate experiments were performed to capture (i) steady-state and (ii) transient cooling of the microdevice in the absence of reactant flow. In all experiments, thermocouples were placed ~4 mm upstream and downstream of the packaging to monitor coolant flow entering and exiting the chip, while a third thermocouple monitored chip temperature via the chip's sensor port. Coolant flowmeters and thermocouples were calibrated to determine associated measurement uncertainties, $T_i = T_i \pm \Delta e_c$ and $Q_c = Q_c \pm \Delta e_v$.

In the first experiment, a constant coolant flowrate of 73.4 cm^3 min^{-1} at 277 K was supplied to the initially ambient-temperature chip, and temperatures were monitored at regular time intervals until the steady-state chip temperature of 278 K was reached. Temperature measurements combined with coolant flowrates allowed calculation of the net rate of heat addition to the coolant fluid from the relation:

$$q = Q_c \rho_c C_{p,c} (\Delta T_{\text{coolant}}) \quad \text{where} \quad \Delta T_{\text{coolant}} = T_{c,\text{in}} - T_{c,\text{out}} \pm \sqrt{2} \cdot \Delta e_T \qquad (5)$$

From error propagation theory, we may calculate the resulting uncertainty as

$$\Delta e_Q = \rho_c C_{p,c} \cdot \sqrt{\left(T_{c,\text{in}} - T_{c,\text{out}}\right)^2 \cdot \Delta e_v^2 + Q_c^2 \cdot 2 \cdot \Delta e_T^2} \qquad (5a)$$

Owing to the relatively small thermal mass of the silicon microdevice (7.6 g) and the insulating nature of the Tefzel© packaging assembly, calculated heat removal rates were the same order-of-magnitude as measurement uncertainty. Despite the measurement uncertainty, the experimental data did follow the expected trendline (Figure 6b).

Multiple measurements of steady-state chip temperatures and cooling inlet/outlet temperatures were made as well. For each steady-state measurement, heat removal rate, q, was calculated from Eq. 5 with its associated uncertainty estimated from Eq. 5a. Assuming uniform chip temperature and a heat-transfer surface area of 2.35 × 10^{-5} m^2, the heat transfer coefficient can be estimated from the following relation,

$$h_a = \frac{q}{A_c\left(\Delta T_{\text{chip}}\right)}, \quad \text{where}$$

$$\Delta T_{\text{chip}} = T_{\text{chip}} - \left(\frac{T_{\text{c,in}} + T_{\text{c,out}}}{2}\right) \pm \sqrt{3} \cdot \Delta e_T \qquad (6)$$

with the resulting error,

$$\Delta e_{h_a} = \frac{1}{A_c}\sqrt{\left(\frac{\Delta e_Q^2}{\Delta T_{\text{chip}}^2}\right) + \left(\frac{3 \cdot \Delta e_T^2 \cdot q^2}{\Delta T_{\text{chip}}^4}\right)} \qquad (6a)$$

Again, propagation of error results in uncertainties of the same order-of-magnitude as calculated heat-transfer coefficients, as a dual result of low overall heat addition and low temperature gradients (Figure 6c). The small size of the microdevice thus serves to amplify experimental error, necessitating either an order-of-magnitude improvement in thermocouple accuracy or an equivalent increase in microsystem size via scale-out.

As stated earlier, chip temperature was monitored via a single thermocouple assuming near-isothermal operation. The assumption that the chip is isothermal is supported by design-level analysis. As was stated earlier, chip temperature was monitored via a single thermocouple assuming near-isothermal operation, and so direct measurement of thermal nonuniformities was not possible. In addition, the packaging chuck and condensation on exposed surfaces during operation effectively prevented more detailed analysis of thermal gradients across the microdevice via thermal imaging methods in the present study. Instead, the effective thermal resistances that describe lateral heat conduction within the silicon chip and outward heat conduction through the Tefzel package were calculated and compared. The lateral thermal resistance of the silicon chip is increased by its low cross sectional area but reduced by silicon's high thermal conductivity of ~130 W m^{-1} K^{-1}; the outward thermal resistance of the package is reduced by its high cross-sectional area and increased by its low thermal conductivity of ~0.24 W m^{-1} K^{-1}. On balance, the thermal resistance of the package exceeds that of the silicon chip by about an order of magnitude, and so only a small fraction of the ~20 K temperature difference between the chip and the ambient occurs across the silicon chip itself, in agreement with the isothermal assumption.

Flow regime observations

During the preliminary two-phase experiments described earlier, two flow regimes were observed over the range of helium and water flow rates investigated. At low gas flows, the gas–liquid interface appeared static, with liquid preferentially flowing along and near the walls of the channel (Figure 7). Liquid appeared to flow through a network of wetted pore throats, in similar fashion to the macroscale "trickling-flow" regime, with few visible fluctuations. This regime was identical to the "annular flow" reported by Losey et al.[50] and Wada et al.[39] in similar postbed microreactors. At elevated gas flows, the gas–liquid interface fluctuates rapidly, as pore throats oscillate between wet and dry operation. This regime was similar to the "churn flow" re-

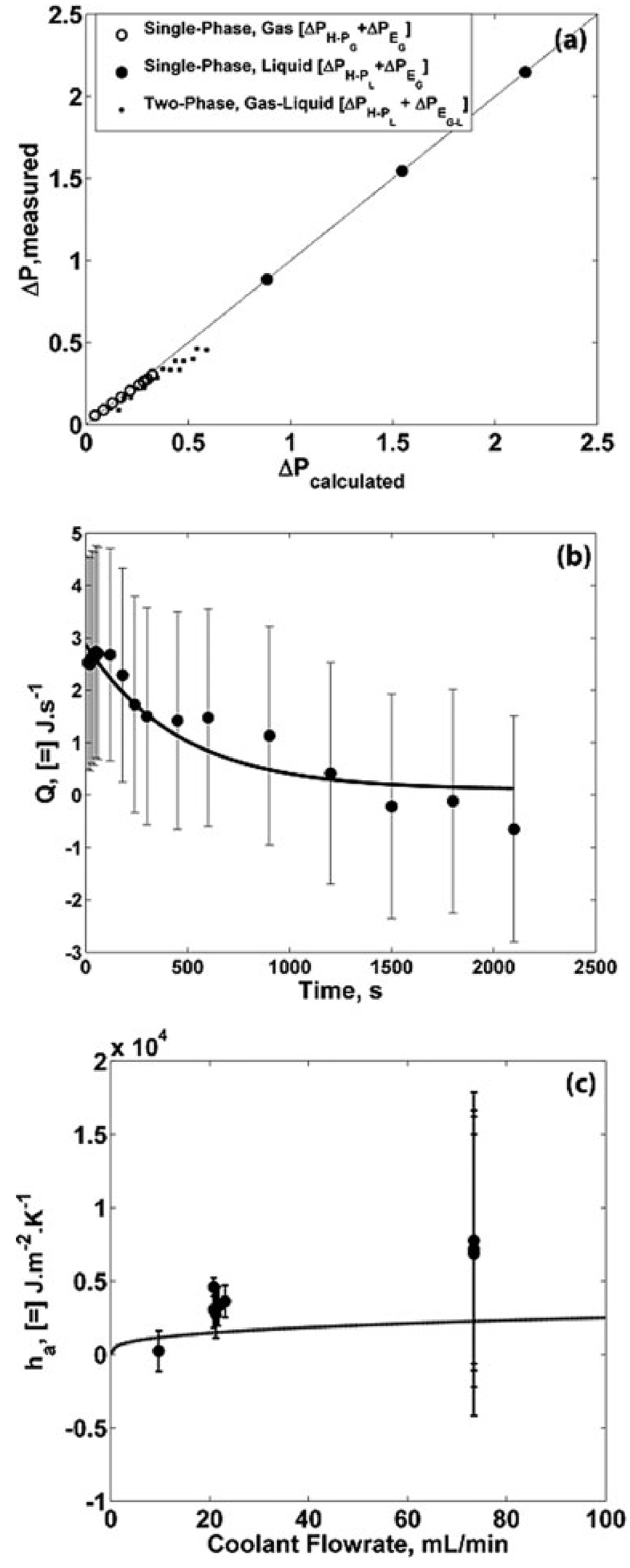

Figure 6. Evaluation of chip performance.

(a) Single- and two-phase pressure drop parity plot; (b) transient cooling of microdevice; (c) calculated heat transfer coefficient from steady-state cooling experiments. Trendlines calculated from Eqs. 5 and 6.

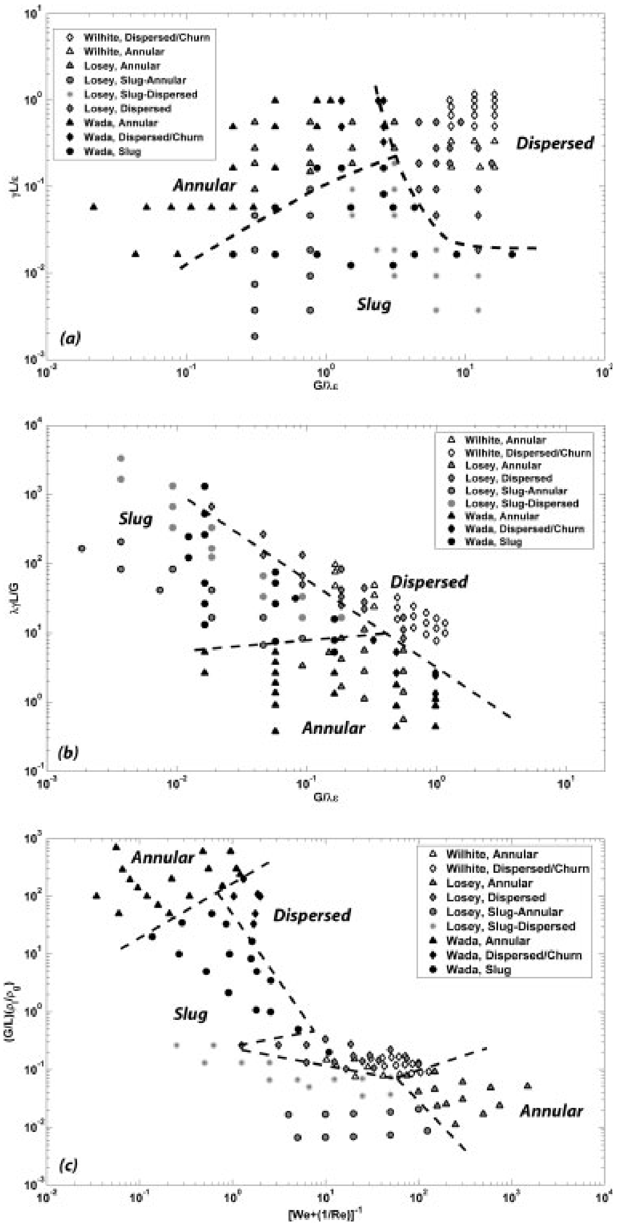

Figure 7. Summary of hydrodynamic observations in structured post-bed microreactors (present work.[39,50]

(a) Baker coordinate map, mapping corrected gas space velocity vs. corrected liquid space velocity; (b) Charpentier and Favier coordinate map, mapping corrected ratio of liquid-to-gas space velocity ratio to corrected gas space velocity; (c) Talmor coordinate map, mapping corrected gas–liquid space velocity ratio vs. dimensionless function of Weber and Reynolds #.

gime reported by Wada et al.[39] and the "dispersed flow" reported by Losey et al.[50] In this flow regime, fluctuations in the gas–liquid interface spanned individual pore throats, but not the entire column diameter. It is important to note that under all singlet-oxygen generating conditions reported, only the annular flow regime occurred.

Another flow regime has been reported in previous studies of microscale postbed reactors, specifically the "slug flow" regime, characterized by channel-spanning gas plugs and observed by both Wada et al.[39] and Losey et al.[50] The presently obtained flow regime data is summarized with that of Wada et al.[39] and Losey et al.[50] using conventional flow regime maps (Figure 7). Three flow regime maps were used; (i) the Baker coordinate map[51] commonly employed for open pipe flow, (ii) the Charpentier-Favier coordinate map,[52] which is popular for trickle-bed (packed pipe) flow, and (iii) the Talmor coordinate map,[53] also used for trickle-bed systems.

Singlet-oxygen production

The resulting miniaturized trickle-bed reactor system was investigated for singlet-delta oxygen production over a range of operating conditions, including outlet pressure, inlet flowrate, and chlorine mole fraction. Singlet-delta oxygen yield was calculated from spectrometer data and chip effluent values extrapolated from singlet-delta oxygen deactivation models accounting for losses en route to the optical sensing region. Optimal performance corresponded to a singlet-delta oxygen yield of 78% at the chip's outlet, occurring at a total gas flowrate of 75 sccm and an outlet pressure of 13 kPa. This compares favorably with maximum yields of 73% reported to date for state-of-the-art macroscale singlet-oxygen generators. Complete details of the data analysis including determination of singlet-oxygen yields over a broad range of gas flows, compositions, and pressures and comparisons with model predictions are presented in a separate report.[21]

Discussion

Preliminary measurements for pressure drop and heat transfer demonstrate the applicability of established equations for laminar flow in the design of microscale systems. The empirical relationship of Ergun[48] agrees well with single-phase pressure drop data, and the relationship of Larkins et al.[49] agrees well with the two-phase pressure drop measurements. During operation some nonuniformity of flow patterns between individual channels was observed, indicating variations in inlet pressure and gas/liquid feedrates from channel to channel. As discussed in the design section of the manuscript, flow uniformity improves with increasing pressure drop across the pressure-drop channels (within the distribution zone) relative to the pressure drop of the reaction channels, assuming that all pressure drop channels are identical. In theory, increasing the ratio of pressure drops may be accomplished by increasing the lengths of the pressure-drop channels, decreasing the widths of the pressure-drop channels, or redesigning the reaction channels themselves to reduce their flow resistance. The assumption that all pressure-drop channels are identical introduces a significant fabrication challenge, however. In the present design, the pressure-drop channel features are already sufficiently small (25 μm width × 20 μm depth) that the few micron scale errors common to the microfabrication process can be a noticeable fraction of the channels' hydraulic diameter; variations in diameter limit the reproducibility of the resulting flow resistances. Therefore, in practice the best way to increase the flow resistance of the pressure drop channels would be both increase their width slightly to improve uniformity while also increasing their length so that the net effect is an increase in flow resistance. For a fixed amount of variation in the feature sizes, a suggested doubling of the channel width would reduce the relative error (fractional variation) in the channel width by a factor of two. The reduced relative error in width reduces the relative error in the flow resistance by an amount that is to lowest order also approximately equal to a factor of two. (For example, a 3 μm error corresponds to about a ±40% error in resistance on a 20–25 μm wide channel, but only about a ±23% error on a 40–50 μm wide channel.) Coupling this increase in channel width with a sufficient increase in channel length to achieve a pressure drop of 3600 torr (~10 times that observed within the reaction channels) would correspond to pressure-drop channel dimensions of 50 μm width × 40 μm depth × 18 mm length. The third approach, redesigning the reaction channels to reduce their flow resistance, would also allow the pressure-drop channels to provide greater control over flow distribution. Bed pressure drops could be substantially reduced by increasing the void fraction/packing density. However, this approach comes at the potential cost of altering hydrodynamic regime and reducing gas–liquid mass transfer rates.

Hydrodynamic observations and attempts to "map" flow regimes according to macroscale conventions illustrate significant differences for microscale systems. Figure 7 summarizes the presently obtained flow regime data alongside that of Wada et al.[39] and Losey et al.[50] obtained in similar packed-bed systems, using coordinate maps following (a) the Baker coordinate map[51] commonly employed for open pipe flow, (b) the Charpentier-Favier coordinate map,[52] which is popular for trickle-bed (packed pipe) flow, and (c) the Talmor coordinate map.[53] By comparing flow regime data obtained in the present work with those previously reported, we can comprehensively evaluate conventional flow regime map prediction of annular and dispersed flow regimes (observed in the present work) as well as slug flow, previously observed by both Losey et al.[50] and Wada et al.[39] In all three cases, experimental data does not follow trends established in the literature for macroscale trickle-beds. Suggested boundaries separating individual flow regimes are superimposed over the experimental data in Figure 7. Both the Baker and Charpentier coordinate maps are found capable of grouping like flow regimes with relatively smooth boundaries, whereas the Talmor map requires much more complex boundaries. In all three cases, data corresponding to the annular flow regime proved difficult to separate from the dispersed regime. The Charpentier-Favier coordinate map indicates that the boundary separating annular flow and slug flow in microscale packed-beds occurs at a near-constant liquid-to-gas flow ratio; that is, increasing gas flowrate does not reduce the stability of the annular flow regime. This is in constrast to conventional packed-bed data, where increased gas flowrate results in lower liquid-to-gas flow ratio necessary for trickling-to-pulsing transition. The Charpentier-Favier and Baker coordinate maps both indicate that the dispersed flow regime occurs at the limit of large gas and liquid flow rates, analogous to conditions for dispersed-bubble flow in macroscale trickle-beds.

In the case of the Baker coordinate map, it is worth noting that annular regime is observed in microchannel systems at conditions corresponding to a dispersed regime in macroscale or conventional systems. Such shifts in expected flow regime are a direct result of substantial changes in the relative strength of capillary and gravity forces which dictate flow regime, reviewed in detail by Günther and Jensen.[54] The present analysis serves to illustrate the need to develop more accurate hydrodynamic models capable of predicting flow regime over a broad (10^{-3}–10^{-1} m) range of hydraulic diameters. It has been well-established that appropriate selection and/or manipulation of flow regime can lead to substantial improvements in conventional packed-bed reactor performance.[55–57] Recent studies in microchannel systems demonstrated equivalent enhancement in reactor performance by utilizing the churn flow regime in lieu of the annular flow regime used in the present work.[58] Thus, more accurate flow regime models for microchannel systems would enable manipulation of flow regime to further enhance interfacial mass transport and, in turn, microreactor performance.

Additional refinements in packed-bed models are expected to improve design of subsequent microscale trickle-bed reactors. Analysis of the estimated reactant molecular diffusivities indicate that the Bodenstein numbers span O(10^1–10^2) over the range of conditions investigated (Table 1), suggesting the presence of secondary dispersive effects. The present experimental system prevented experimental investigation of actual fluid-phase dispersion, owing to the relatively large volumes associated with both upstream and downstream plumbing volume and the presence of the gas–liquid disengagement zone. Thus, the inclusion of axial dispersion is expected to further refine model accuracy. Additional improvement in model accuracy is expected by including the rate expressions for liquid-phase deactivation of singlet-oxygen product. The presently used model accounts for gas-phase deactivation kinetics only via the simplifying assumption of negligible liquid-phase deactivation, owing to thin reaction depths within the liquid phase (~1×10^{-6} cm).

More critical is the need for re-evaluation of gas–liquid contacting areas within the microdevice. Model values were based upon the previously reported gas–liquid contacting areas obtained for the cyclohexane-hydrogen system in a similar microscale packed-bed under dispersed flow regime.[50] Visual confirmation of an annular flow regime during singlet-delta oxygen generation suggests that actual gas–liquid contacting areas encountered in the present work may be significantly smaller than expected. Analysis of flow regime maps in Figure 7 suggest that by increasing liquid flowrate (for a given constant gas flowrate), onset of the dispersed flow regime will occur resulting in improved gas–liquid mixing.

Assuming purely annular flow (instead of dispersed-flow) in the presence of the packing structure, and assuming model values for $\varepsilon_l = 0.08$, then w_{film} ~65 μm and the minimum and maximum liquid–gas contacting areas can be estimated from geometry (Figure 8) as:

$$a_{\mathrm{l-g}}^{\min} = \frac{2 \cdot \left(\frac{t_p}{z_p}\right) \cdot L_{\mathrm{pbr}} \cdot h_{\mathrm{pbr}}}{2 \cdot \left(\varepsilon_{\mathrm{pbr}}\right) \cdot \left(w_{\mathrm{pbr}} - w_{\mathrm{film}}\right) \cdot L_{\mathrm{pbr}} \cdot h_{\mathrm{pbr}}} = \frac{\left(\frac{20}{78}\right)}{(0.4)\cdot(650-65)} = 1100\ \mathrm{m}^{-1}$$

$$a_{\mathrm{l-g}}^{\min} = \frac{2 \cdot \left(\frac{t_p}{z_p}\right) \cdot L_{\mathrm{pbr}} \cdot h_{\mathrm{pbr}}}{2 \cdot \left(\varepsilon_{\mathrm{pbr}}\right) \cdot \left(w_{\mathrm{pbr}} - w_{\mathrm{film}}\right) \cdot L_{\mathrm{pbr}} \cdot h_{\mathrm{pbr}}} = \frac{\left(\frac{86}{156}\right)}{(0.4)\cdot(650-65)} = 2400\,\mathrm{m}^{-1}$$

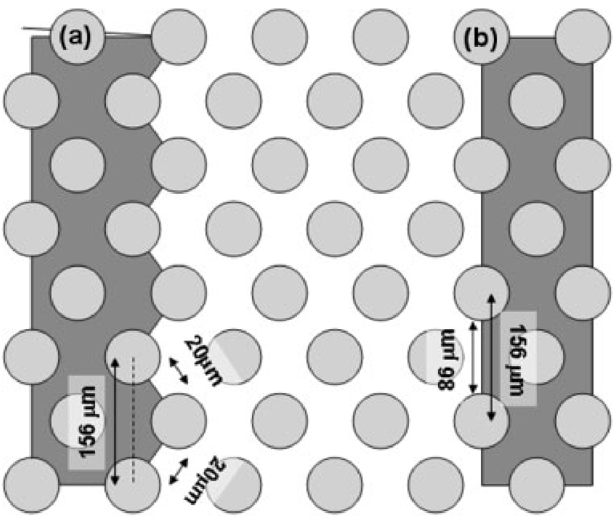

Figure 8. Estimation of gas–liquid mass transfer area, assuming stagnant, and annular flow.

(a) minimum pore throat; (b) maximum pore throat.

These numbers suggest interfacial transfer areas significantly lower than the value of 5000^{-1} m used in the reactor design model. This illustrates the need for continued efforts to accurately predict flow regimes within the microscale packed-bed during the design phase as well as the need to develop accurate experimental methods for measuring gas–liquid mass transfer. The present microdevice represents a first step towards achieving both of these goals. Further reduction in the size of the gas–liquid disengagement volume for the present microdevice would improve the accuracy of such mass-transfer measurements.

Although not exploited in the present work, the use of packing elements formed via reactive extrusion (e.g., DRIE) from two-dimensional lithography mask features also allows complete control over placement and shape of each element without imposing limits on total element quantity. This packed-bed design strategy represents a logical extension of, and improvement over, previous fundamental studies in structured two-dimensional beds constructed from conventional machining.[59]

Conclusions

This article reports the complete bottom-to-top modeling, design, construction, and flow testing of a fully miniaturized trickle-bed reactor system. This system successfully integrates gas–liquid distributors, structured packed beds, gas–liquid separator, and cooling channels into one compact microscale device. The resulting device was demonstrated for the exothermic reaction of chlorine gas and BHP to produce singlet-delta oxygen. This chemistry represented an aggressive test of microchemical systems capabilities, owing to the highly corrosive and reactive reagents, high heat of reaction, significant gas–liquid mass transport limitations, and subsequent deactivation challenges of gaseous product. Preliminary experiments verified the accurate design of gas and liquid distributors, gas–liquid separator, and cooling channels. The applicability of well-established pressure-drop correlations, specifically those of Ergun[48] and Larkins et al.[49] was verified with water and helium fluids. Observations of the gas–liquid flow regimes within the structured microscale packed-bed system were compared with conventional, that is, macroscale, regime maps. This comparison identified a significant disconnect between macroscale and microscale flow regime boundaries in gas–liquid packed-beds, which provides a basis for further hydrodynamic and interfacial mass transport studies.

Experimental data verified that the microdevice was capable of producing singlet-delta oxygen in measurable quantities, in general agreement with packed-bed reactor models used for the presented design methodology.[20] Analysis of molecular diffusivities suggests further improvement in model accuracy may be achieved with inclusion of second-order dispersion terms. The resulting microscale trickle-bed system is also expected to serve as a flexible tool for relating bed and packing geometry to gas–liquid hydrodynamics and mass transport, and demonstrates a significant step towards realizing fully integrated, miniaturized gas–liquid and gas–liquid-solid microreactor systems.

Acknowledgments

Microfabrication of all devices was performed in the Microsystems Technology Laboratories (MTL) at M.I.T. The authors wish to acknowledge Dr. Hanqing Li's contributions to the device fabrication and Dr. Terry Rawlins's, Dr. Seonkyung Lee's, and Dr. Steve Davis's contributions to the spectroscopic measurements. This work was funded by the Tactical Technology Office at DARPA, the Missile Defense Agency (MDA), and the Air Force Research Laboratory (AFRL) (DARPA Order No. T171/00, Program Code: 4G10; Issued by DARPA/CMO under Contract No. MDA972-04-C-0140). The views and conclusions contained in this document are those of the authors and should not be interpreted as representing the official policies, either expressed or implied, of the Defense Advanced Research Projects Agency or the U.S. Government.

Notation

a = inter-phase transfer area (m^2)
C_p = specific heat (J g^{-1} K^{-1})
d = diameter (cm)
D = packed-bed dispersion coefficient (cm^2 s^{-1})
D_{A-B} = molecular diffusivity of solute A in solvent B (cm^2 s^{-1})
Δe_i = uncertainty in calculated value i
h_a = convection heat transfer coefficient
k = thermal conductivity
L = length (cm)
P = absolute pressure (kPa)
Q = volumetric flowrate (cm^3 s^{-1})
q^+ = rate of heat addition due to chemical reaction (J s^{-1})
q^- = rate of heat removal due to coolant flow (J s^{-1})
T = Temperature (K)
t_p = pore throat (m)
v_l = fluid velocity of phase i (cm s^{-1})
w_i = width of fluid i film
z_p = pore spacing, along axial length of bed

Symbols

ε = void fraction, dimensionless
μ = viscosity (kg m^{-1} s^{-1})
θ = wetting angle (radians)

ρ = density (kg m^{-3})
σ = surface tension (N m^{-1})

Dimensionless numbers

$N_{Bo} = \frac{vL}{D} =$ Bodenstein number
$N_{Gr} = \frac{L^3 \rho_{air}^2 g \beta \Delta T}{\mu_{air}^2} =$ Grashoff number
$N_{Nu} = \frac{h_a D}{k} =$ Nusselt number
$N_{Pr} = \frac{C_p \mu}{k} =$ Prandtl number
$N_{Re} = \frac{\rho v D}{\mu} =$ Reynold's number
$N_{We} = \frac{\rho v^2 D}{\sigma} =$ Weber number
$\gamma = \left[\left(\frac{\rho_g}{\rho_{air}} \right) \left(\frac{\rho_l}{\rho_{water}} \right) \right]^{1/2}$, Lockhart-Martinelli parameter for correcting gas, liquid space velocities (In Figure 7).
$\lambda = \left(\frac{\sigma_{water}}{\sigma_l} \right) \left[\left(\frac{\mu_l}{\mu_{water}} \right) \left(\frac{\rho_{water}}{\rho_l} \right)^2 \right]^{1/3}$, flow parameter for Baker Plot (Figure 7c).

Subscripts

c = cooling channels
cap = capillary pore in gas-liquid separator
g = gas phase
l = liquid phase
l-g = liquid-gas interface
p = packing element
pbr = packed-bed region
pdc = pressure drop channels

Literature Cited

1. Dittrich PS, Tachikawa K, Manz A. Micro total analysis systems. Latest advancements and trends. *Anal Chem*. 2006;78:3887–3907.
2. Vilkner T, Janasek D, Manz A. Micro total analysis systems. Recent developments. *Anal Chem*. 2004;76:3373–3385.
3. El-Ali J, Sorger PK, Jensen KF. Cells on chips. *Nature*. 2006;442: 403–411.
4. Holladay JD, Wang Y, Jones E. Review of developments in portable hydrogen production using microreactor technology. *Chem Rev*. 2004;104:4767–4790.
5. Jensen KF, Microreaction engineering—is small better? *Chem Eng Sci*. 2001;56:293–303.
6. deMello AJ. Control and detection of chemical reactions in microfluidic systems. *Nature*. 2006;422:394–402.
7. Pennemann H, Watts P, Haswell SJ, Hessel V, Loewe H. Benchmarking of microreactor applications. *Org Process Res Dev*. 2004; 8:422–439.
8. Jahnisch K, Hessel V, Lowe H. Baems M. Chemistry in microstructured reactors. *Angew Chem Int Ed Engl*. 2004;43:406–446.
9. Hessel V, Hardt S, Lowe H. *Chemical Micro Process Engineering: Fundamentals, Modeling and Reactions*. Weinheim: Wiley-VCH, 2004.
10. Stankiewicz AI, Moulijn JA. Process intensification: transforming chemical engineering. *Chem Eng Prog*. 2000;1:22–34.
11. Jensen KF. Silicon-based microchemical systems: characteristics and applications. *MRS Bull*. 2006;31:101–107.
12. Ajmera SK, Losey MW, Jensen KF, Schmidt MA. Microfabricated packed-bed reactor for phosgene synthesis. *AIChE J*. 2001;47:1639–1647.
13. Velasquez-Garcia LF, Hill TF, Wilhite BA, Rawlins WT, Lee S, Jensen KF, Epstein AH, Livermore C. A MEMS singlet-oxygen generator. I. Design and fabrication. *J Microelectromech Syst*. 2007;16:1482–1491.
14. Ledermann N, Baborowksi J, Muralt P, Xantopoulos N, Tellenbach JM. Sputtered silicon carbide thin films as protective coatings for MEMS applications. *Surf Coat Technol*. 2000;125:246–250.
15. DeMas N, Gunther A, Schmidt MA, Jensen KF. Microfabricated multiphase reactors for the selective direct flourination of aromatics. *Ind Eng Chem Res*. 2003;42:698–710.
16. Thorsen T, Maerkl SJ, Quake SR. Microfluidic large-scale integration. *Science*. 2002;298:580–584.
17. DeMas N, Gunther A, Kraus T, Schmidt MA, Jensen KF. Scaled out multilayer gas-liquid microreactor with integrated velocimetry sensors. *Ind Eng Chem Res*. 2005;44:8997–9013.
18. Arana LR, Schaevitz SB, Franz AJ, Schmidt MA, Jensen KF. A microfabricated suspended-tube chemical reactor for thermally efficient fuel processing. *J Microelectromech Syst*. 2003;12:600–612.
19. Sahoo HR, Kralj JG, Jensen KF. Multi-step continuous flow microchemical synthesis involving multiple reactions and separations. *Angew Chem Int Ed Engl*. 2007;46:5704–5708.
20. Wilhite BA, Livermore C, Gong Y, Epstein AH, Jensen KF. Design of a MEMS-based microchemical oxygen-iodine laser (μCOIL) system. *IEEE J Quantum Electron*. 2004;40:1041.
21. Hill TF, Velasquez-Garcia LF, Wilhite BA, Rawlins WT, Lee S, Jensen KF, Epstein AH, Livermore C. A MEMS singlet-oxygen generator—Part II: Testing. *J Microelectromech Syst*. 2007;16:1492–1505.
22. Wasserman HH, Murray RW. *Singlet Oxygen*. New York: Academic Press, 1979.
23. Clennan EL. New mechanistic and synthetic aspects of singlet oxygen chemistry. *Tetrahedron*. 2000;56:9151–9179.
24. Moseley H. The scientific basis of PDT. *SPIE*. 2003;5287:35–38.
25. Takeda S, Nanri K, Fujioka T. Industrial and reverse-industrial applications of COIL. *SPIE*. 1996;702:191–194.
26. von Bulow H, Schall WO. Oxygen-iodine lasers for industrial applications. *SPIE*. 1995;2502:258–265.
27. Powell J. *CO_2 Laser Cutting*, 2nd ed. New York: Springer, 1998.
28. Endo M, Wani F, Nagatomo S, Sugimoto D, Nanri K, Tadeka S, Fujioka T. Development of industrial COIL. *SPIE*. 1998;3574:253–264.
29. McDermott WE, Pchelkin NR, Bernard DJ, Bousek RR. An electronic transition chemical laser. *Appl Phys Lett*. 1978;32:469–473.
30. Dahlberg MR, Cochrane ME. Tactical high energy laser (THEL) as a weapon system in future theater air and missile defense (TAMD). *SPIE*. 1999;3612:111–116.
31. Manke GC, Cooper CB, Dass SC, Madden TJ, Hager GD. A multiwatt all gas-phase iodine laser (AGIL). *IEEE J Quantum Electron*. 2002;39:995–1002.
32. Henshaw TL, Madden TJ, Herbelin JM, Manke GC II, Anderson BT, Tate RF, Hager GD. Measurement of gain on the 1.315 μm transition of atomic iodine produced from the $NCl(a^1\Delta) + I_2(^2P_{3/2})$ energy transfer reaction. *SPIE*. 1999;3612:147–151.
33. Carroll DL, Solomon WC. Electricoil: an advanced chemical iodine laser concept. *SPIE*. 2001;4184:40–44.
34. Kendrick KR, Helms CA, Quillen B, Copland RJ. Quantitative determination of oxygen yield in a chemical oxygen-iodine laser. *SPIE*. 1998;3268:125–129.
35. Kwirandt GR, Schall WO. Basic experiments on the production of $O_2(^1\Delta)$. *SPIE*. 1995;2502:331–337.
36. Zagidullin MV, Nikolaev VD, Khvatov NA, Svistun MI. The sub- and supersonic coils driven by jet type singlet oxygen generator. *SPIE*. 1998;3574:246–252.
37. Truesdell KA, Lamberson SE, Hager GD. *Phillips Laboratory COIL Technology Overview*. 1993;AIAA92–3003.
38. Losey MW, Schmidt MA, Jensen KF. Microfabricated multiphase packed-bed reactors: characterization of mass transfer and reactions. *Ind Eng Chem Res*. 2001;40:2555–2562.
39. Wada Y, Schmidt MA, Jensen KF. Flow distribution and ozonolysis in gas-liquid multichannel microreactors. *Ind Eng Chem Res*. 2006; 45:8036–8042.
40. Gunther A, Jhunjhunwala M, Thalmann M, Schmidt MA, Jensen KF. Micromixing of miscible liquids in segmented gas-liquid flow. *Langmuir*. 2005;21:1547–1555.
41. London AP, Ayon AA, Epstein AH, Spearing SM, Harrison T, Peles Y, Kerrebrock JL. Microfabrication of a high pressure bipropellant rocket engine. *Sens Actuators A Phys*. 2001;92:351–357.
42. Gianetto A, Silveston PL. *Multiphase Chemical Reactors*. New York: Springer-Verlag, 1986.
43. Amador C, Gavriilidis A, Angeli P. Flow distribution in different microreactor scale-out geometries and the effect of manufacturing tolerances and channel blockage. *Chem Eng J*. 2004;101:379–390.
44. Sieder EN, Tate GE. Heat transfer and pressure drop of liquids in tubes. *Ind Eng Chem*. 1936;28:1429–1436.
45. Rawlins WT, Lee S, Davis SJ. Singlet oyxgen measurements for micro-coil. PSI-2918/TR-2096, May 2006.
46. Inoue T, Schmidt MA, Jensen KF. Microfabricated multiphase reactors for the direct synthesis of hydrogen peroxide from hydrogen and oxygen. *Ind Eng Chem Res*. 2007;46:1153–1160.

47. Ratner DM, Murphy ER, Jhunjhunwala M, Snyder DA, Jensen KF, Seeberger PH. Microreactor-based reaction optimization in organic chemistry-glycosylation as a challenge. *Chem Commun*. 2005;5:578–583.
48. Ergun S. Fluid flow through packed columns. *Chem Eng Prog*. 1952;48:89–94.
49. Larkins RP, White RR, Jeffrey DW. Two-phase concurrent flow in packed beds. *AIChE J*. 1961;7:231–236.
50. Losey MW, Jackman RJ, Firebaugh SL, Schmidt MA, Jensen KF. Design and fabrication of microfluidic devices for multiphase mixing and reaction. *J Microelectromech Syst*. 2002;11:709–717.
51. Baker, D. Simultaneous flow of oil and gas. *Oil Gas J*. 1954;53:183–195.
52. Charpentier JC, Favier M. Some liquid holdup experimental data in trickle-bed reactors for foaming and nonfoaming hydrocarbons. *AIChE J*. 1975;21:1213–1218.
53. Talmor E. Two-phase downflow through catalyst beds. *AIChE J*. 1997;23:868.
54. Gunther A, Jensen KF. Multiphase microfluidics: from flow characteristics to chemical and materials synthesis. *Lab Chip*. 2006;6:1487–1503.
55. Wilhite BA, Wu R, Huang X, McCready MJ, Varma A. Enhancing performance of three-phase catalytic packed-bed reactors. *AIChE J*. 2001;47:2548–2556.
56. Wilhite BA, Huang X, McCready MJ, Varma A. Effects of induced pulsing flow on trickle-bed reactor performance. *Ind Eng Chem Res*. 2003;42:2139–2145.
57. Boelhouwer JG, Piepers HW, Drinkenburg AAH. Liquid-induced pulsing flow in trickle-bed reactors. *Chem Eng Sci*. 2002;57:3387–3399.
58. Bakker JJ, Groendijk WJ, de Lathouder KM, Kapteijn F, Moulijn JA, Kreutzer MT, Wallin SA. Enhancement of catalyst performance using pressure pulses on macroporous structured catalysts. *Ind Eng Chem Res*. 2007;46:8574–8583.
59. Melli TR, Scriven LE. Theory of two-phase cocurrent downflow in networks of passages. *Ind Eng Chem Res*. 1991;30:951–957.

Manuscript received Sept. 5, 2007, revision received Mar. 31, 2008, and final revision received May 14, 2008.